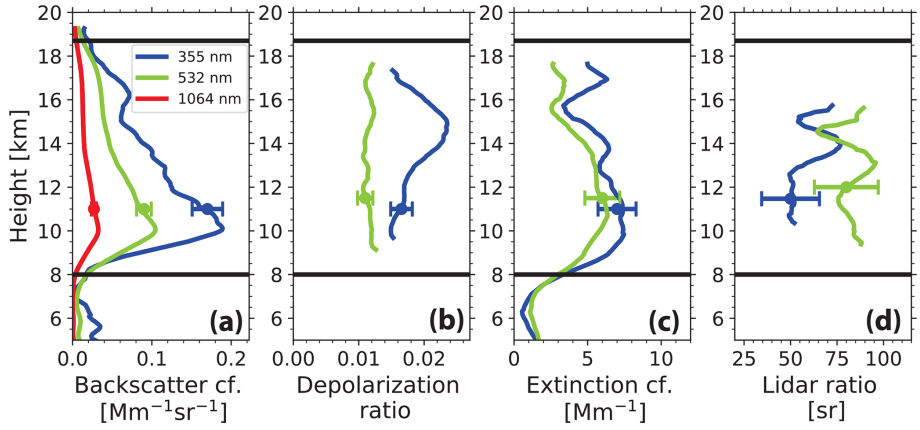

Figure 4. Profiles of optical properties (24 h mean values) of the wildfire smoke layer on 11 December 2019. Base and top heights of the smoke layer are indicated by black horizontal lines. **(a)** Particle backscatter coefficient at three wavelengths, **(b)** particle linear depolarization ratio at 355 and 532 nm, **(c)** smoke extinction coefficient at 355 and 532 nm, and **(d)** respective smoke extinction-to-backscatter ratio (lidar ratio) are shown. All basic lidar signal profiles were strongly smoothed with vertical window lengths of 2000 m to strongly reduce the signal noise. Error bars indicate the estimated uncertainties (1 standard deviation). More details are given in Ohneiser et al. (2021).

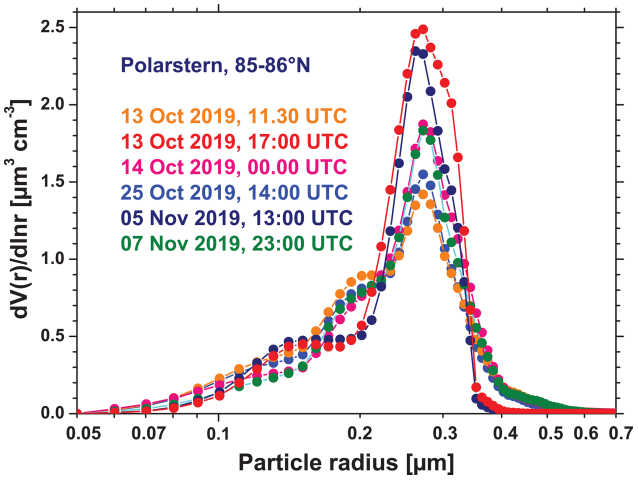

Figure 5. Size distributions of the stratospheric smoke particles retrieved from the multiwavelength lidar observations on 5 d in October and November 2019. A narrow accumulation mode with particle sizes (diameters) from 400 to 1000 nm and a weak Aitken mode to the left are typical for aged wildfire smoke particles.

no time for particle aging. Then, the particles widely keep their original, non-spherical shapes and thus produce large depolarization ratios of about 20 % at 532 nm.

Figure 5 presents several volume size distributions of the smoke particles. The volume size distributions were obtained from the Polly observation by applying the lidar inversion method to the layer mean three backscatter and two extinction coefficients (Veselovskii et al., 2002). As typical for aged wildfire smoke, a well-defined accumulation mode was found. A distinct coarse mode was absent. The findings agree well with in situ observations of aged smoke transported over long distances (Fiebig et al., 2003; Petzold et al., 2007; Dahlkötter et al., 2014).

An overview of the smoke conditions during the MOSAiC winter half year (October to April) is presented in Fig. 6. Most of the time, the smoke layer was observed between 7 and 17 km height with the backscatter maximum just above the tropopause. A trend of downward movement of the layer is not visible. The maximum extinction coefficients (532 nm) decreased with time from values $> 10\,\mathrm{M\,m^{-1}}$ in October and November to $< 5\,\mathrm{M\,m^{-1}}$ in April 2020 (Fig. 6a).

The AOT in Fig. 6b was computed from the particle backscatter height profiles. The directly determined extinction profiles were too noisy, especially in the upper part of the smoke layer. The 532 nm backscatter coefficients were multiplied with the smoke mean lidar ratio of 85 sr (computed from all smoke observations measured during the winter half year) (Ohneiser et al., 2021). Subsequently, we integrated the extinction values between the smoke layer base and top heights as given in Fig. 4 to obtain the AOT. During the winter months, especially in January to February 2020, polar stratospheric clouds (PSCs) were frequently observed at the top and above the smoke layer, from 17 to 25 km height. We removed these PSC-affected parts from the height profiles of backscatter and extinction coefficients before we calculated the vertical column-integrated smoke optical properties. However, several weak PSCs developed within the smoke layer, and in this case, the backscatter and extinction contributions from these optically thin PSCs were not removed. The PSC-related uncertainty in the 532 nm AOT was estimated to be of the order of 5 % (Ohneiser et al., 2021).

In terms of the 532 nm AOT in Fig. 6b, the perturbation decreased from 0.05–0.12 in October and November to values of 0.03–0.06 in December to the middle of March and dropped to 0.01–0.02 in April 2020. Almost constant AOT

and agricultural fire smoke (organic aerosol). Sulfate aerosol prevails in the near-surface air, whereas OA becomes comparably large in the free troposphere. This was observed during the POLARCAT-IPY and ACCESS CE11 campaigns. Agricultural fires during spring (Europe, Asia) and flaring of natural gas (Russian oil industry) were found to be important sources for BC and OA particles. The fire smoke mixes with anthropogenic haze mainly from Asia during the long-range transport towards the central Arctic, beginning in late winter with peak occurrence in the spring season. Agricultural and forest fires produce BC/OA ratios of typically < 0.1, whereas anthropogenic haze may cause ratios > 0.15.

3.3 Mixed-phase cloud evolution in Arctic haze

Two MOSAiC case studies of aerosol–cloud interaction are presented next. In this section, the evolution of a long-lasting mixed-phase altocumulus layer in Arctic haze within the lower free troposphere is discussed, and, in the next section, we present a cirrus development in the lower part of the UTLS wildfire smoke layer.

The mixed-phase cloud system was shown in Fig. 3e and f. The cloud layer was observed for more than 7 h over the *Polarstern* on 10 December 2019. The dark band in the depolarization ratio panel between 2–3 km height in Fig. 3f indicates the liquid-water-dominated cloud top layer. The increase in the depolarization ratio above the dark zone at the liquid cloud base is caused by multiple scattering at cloud droplets. Favorable conditions with cloud top temperatures around −28.5 °C at 2.6 km height (at 03:00 UTC) were given for heterogeneous ice formation via immersion freezing, i.e., ice nucleation on INPs immersed in the water droplets (Kanji et al., 2017). After nucleation in the cloud top layer, ice crystals grow fast to sizes of 50–100 µm within minutes (Bailey and Hallett, 2012) and immediately start to fall out. As visible in Fig. 3e and f, the crystals formed long virga below the shallow altocumulus layer. The ice crystals partly evaporated on the way down but partly reached the ground as precipitation. The liquid-water-dominated cloud top layer was not depleted at any time during the 7 h period.

About 40 long-lasting mixed-phase cloud events (ice-precipitating shallow altocumulus decks) with durations from 4–30 h were observed from October 2019 to March 2020. Because of their sensitive influence on radiative transfer and the water cycle, they have been the focus of research for more than 15 years (Verlinde et al., 2007; Mauritsen et al., 2011; Morrison et al., 2012; Paukert and Hoose, 2014; Loewe et al., 2017; Andronache, 2018; Eirund et al., 2019). However, because of the complexity of influencing meteorological and aerosol aspects, there are still many open questions concerning their long lifetime, especially of the longevity of liquid-water layers and thus of water droplets in the presence of ice crystals. MOSAiC contributes to this research field by means of combined lidar and radar observations aboard RV *Polarstern*.

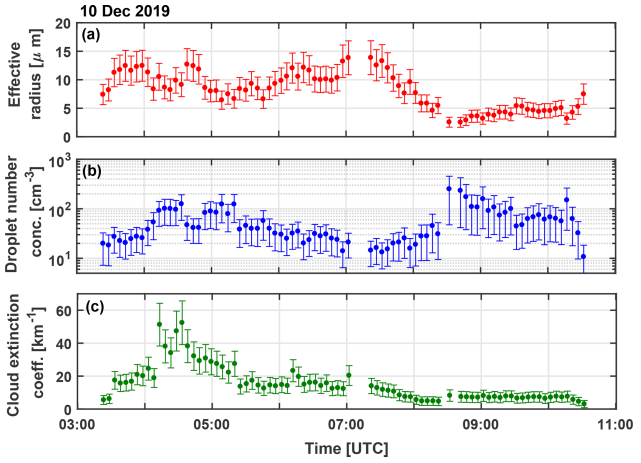

Figure 11. **(a)** Effective radius of cloud droplets, **(b)** cloud droplet number concentration, and **(c)** 532 nm cloud extinction coefficient (single-scattering) at 75 m above cloud base of the altocumulus layer in Fig. 3e and f. The effective radius can be interpreted as the characteristic droplet radius. Error bars indicate the uncertainty. The cloud properties were retrieved by means of the recently introduced dual-FOV polarization lidar technique.

We applied our recently developed dual-FOV polarization lidar method (Jimenez et al., 2020a, b) to derive the microphysical properties of liquid-water droplets in the cloud top layer. The results are shown in Fig. 11. The dual-FOV lidar technique was originally designed for pure liquid-water cloud observations but can be applied to mixed-phase clouds as long as backscattering by ice crystals is negligible compared to droplet backscattering in the cloud top layer. This condition holds here with ice crystal backscatter coefficients of 5–10 M m^{-1} sr^{-1} in the virga (not shown) and thus probably also in the cloud top layer with droplet backscatter coefficients of the order of 700 M m^{-1} sr^{-1} (not shown). In the case of crystal-to-droplet backscattering of 0.01, the contribution of ice crystals to the observed multiple scattering features, from which the microphysical properties of the droplets are retrieved, can be ignored. Note that the method delivers the time series of droplet effective radius, CDNC, and cloud extinction coefficients in Fig. 11 for the height of 75 m above cloud base. Thus, the properties of freshly formed droplets are mainly observed.

As can be seen, the retrieved CDNC values were around 20 cm^{-3} in the beginning and around 100 cm^{-3} in the cloud base region later on. With increasing CDNC the effective radius (a characteristic droplet size) decreased and vice versa as expected when assuming a constant water vapor reservoir for droplet nucleation. The cloud extinction coefficient showed typical values from 10–20 km^{-1} in the first half of the cloud lifetime. Uncertainties in the lidar products are indicated by error bars (1 standard deviation) and are of the order of 20 %–25 % (cloud extinction coefficient, droplet effective radius) and 50 % (CDNC).

The ice nucleation rate coefficient $J_{\mathrm{het,D}}$ requires information on temperature T and ice supersaturation S_{i}, also shown in Fig. 15c, and parameters describing the ice nucleation potential of the organic material. Also in the case of DIN, laboratory results for leonardite were used (Wang and Knopf, 2011). A more detailed description of smoke INP computation may be found in Ansmann et al. (2021).

Figure 17 provides an overview of all retrieval products necessary to evaluate the potential of smoke particles to serve as INP. From the aerosol lidar observations (backscattering in cloud-free conditions) we obtain estimates for the particle surface area concentration s (Ansmann et al., 2021). We show the aerosol conditions at different days in Fig. 17b (before, during, and after the cirrus event) and used the respective lidar backscatter profiles to estimate the surface area concentration of the smoke particles. It can be concluded that the smoke surface area concentration was in the range of 0.05–0.15 $\mathrm{cm^2\,m^{-3}}$ during the formation of ice crystals at 7–7.5 km and at 9.0–9.5 km in the case of the cirrus layer in Fig. 17a. In Fig. 17b, the estimated number concentration of large smoke particles n_{250} (with radius ≥ 250 nm, lower axis) is also shown. n_{250} may be interpreted as the overall reservoir of potential smoke INPs. It is assumed that larger particles provide better ice nucleation conditions than smaller particles. The uncertainty in the aerosol estimates is about 20 %–25 % (Table 1).

Figure 17c shows the results of the INPC calculations with Eqs. (1) and (2). The range of immersion freezing INPC (i.e., the length of the respective two horizontal bars in Fig. 17c) is obtained by computing $n_{\mathrm{INP,I}}$ with Eq. (1) for Δa_{w} of 0.225 and 0.25. The particle surface area concentration of 0.05 $\mathrm{cm^2\,m^{-3}}$ is used in these computations and Δt is set to 600 s. In the case of the deposition nucleation INPC, the shown INPC range (length of each bar) is obtained by computing $n_{\mathrm{INP,D}}$ with Eq. (2) for the corresponding ice supersaturation values S_{i} from 1.37–1.41 (7–7.5 km height, −55.4 °C) and from 1.41–1.44 (9–9.5 km height, −64 °C). As can be seen, $n_{\mathrm{INP,I}}$ ranged from 1–63 $\mathrm{L^{-1}}$ at both heights (for the same Δa_{w} range), and for $n_{\mathrm{INP,D}}$, we obtained values from 0.4–3 $\mathrm{L^{-1}}$ at 7–7.5 km height and $< 0.01\,\mathrm{L^{-1}}$ at 9–9.5 km height. The uncertainty in these estimates is unspecified. This is the first attempt to estimate aged smoke INP under realistic atmospheric conditions with parameterizations developed under laboratory conditions.

In the final step, we compare the immersion freezing INPC values in Fig. 17c, which can also be interpreted as predicted ice crystal numbers, with estimated ice crystal numbers derived from combined lidar–radar observations. The lidar–radar ICNC retrieval was already explained in Sect. 3.3. In this MOSAiC cirrus closure study, we used the strong and most accurate observations of radar reflectivity in the lower part of the virga zones from 4–7 km height. Since Eqs. (1) and (2) primarily deliver ice crystal nucleation rates (for $\Delta t = 1$ s), we compare nucleation rate values in Fig. 18b. As pointed out by Bühl et al. (2019), the ice crystal downward flux (in $\mathrm{m^{-2}\,s^{-1}}$) is the most direct result of lidar–radar retrievals because besides radar reflectivity, the falling velocity is also measured with the Doppler radar. And this crystal flux rate can be interpreted as the ice nucleation rate as long as crystal–crystal collision and aggregation processes do not change the ice crystal number concentration too much, on the way from the cloud top region (ice nucleation region) to the lower part of the virga zones. However, this assumption may be strongly violated as Mitchell et al. (2018) concluded from CALIPSO lidar observations. They found that the ice crystal number concentration in the virga may be lower by a factor of 3–5 compared to the ICNC values at cloud top. On the other hand, the crystal nucleation rates we discuss below were quite low so that the aggregation effect may have been small (of the order of a factor of 2 or less for this Arctic ice cloud system). Other ICNC influencing effects, e.g., secondary ice formation can be ignored in the case of cold cirrus clouds (Field et al., 2006; Korolev and Leisner, 2020). The low lidar–radar-estimated ICNC values of 40–70 $\mathrm{m^{-3}}$ or 0.04–0.07 $\mathrm{L^{-1}}$ (mean values for the virga between 4–6 km height for the period from 06:00–12:00 UTC, not shown here) and about 150 $\mathrm{m^{-3}}$ or 0.15 $\mathrm{L^{-1}}$ higher up (based on less accurate radar reflectivity measured at 6–7 km height) corroborate the idea that the aggregation-related uncertainty in our lidar–radar estimate of the ice crystal nucleation rate at cloud top may have been low. For the time period from 12:00–14:00 UTC, the lidar–radar retrieval yielded ICNC values of 80–500 $\mathrm{m^{-3}}$ or 0.08–0.5 $\mathrm{L^{-1}}$in the virga layer from 4–6 km height and about 800 $\mathrm{m^{-3}}$ at 7 km height.

In our cirrus closure experiment, the goal is now to check how well the two numbers of the predicted and the estimated ice crystal nucleation rates are in agreement. The question behind this is as follows: can the smoke INP parameterizations reproduce these values given by the lidar–radar observations so that we can conclude that smoke particles most likely controlled the evolution of the cirrus deck and the virga and respective ice crystal microphysical properties? INP parameterization is appropriate even to be used in models to describe the smoke impact on cirrus formation.

As shown in Fig. 18b, the lidar–radar retrieval yielded ice crystal nucleation rates of 10–200 $\mathrm{m^{-3}\,s^{-1}}$ and 50–1000 $\mathrm{m^{-3}\,s^{-1}}$ (derived from the crystal flux observations between 4 and 6 km height) for the cirrus period from 06:00–12:00 UTC and 12:00–14:00 UTC, respectively. The prediction (based on INP retrieval with Eq. (1) for $\Delta t = 1$ s) reveals 1–100 $\mathrm{m^{-3}\,s^{-1}}$ at cirrus top layer level. This can be regarded as a reasonable agreement keeping in mind that the particle surface area concentrations may have been underestimated, strong updrafts may have occurred causing significantly higher Δa_{w} values than 0.25 (at a value of $\Delta a_{\mathrm{w}} = 0.27$ we obtain an order of magnitude higher nucleation rates), or leonardite is not representing well the organic material in the liquid shell of the smoke particles. With Pahokee peat parameters we obtain a factor of 3 higher ice crystal nucleation rates (or INPC values).